

# Incorporating the effects of 3D radiative transfer in the presence of clouds into two-stream radiation schemes

ROBIN J HOGAN <sup>\*</sup> AND JONATHAN K P SHONK

*Department of Meteorology, University of Reading, Reading, Berkshire, UK.*

## ABSTRACT

This paper presents a new method for representing the important effects of horizontal radiation transport through cloud sides in two-stream radiation schemes. Ordinarily, the radiative transfer equations are discretized separately for the clear and cloudy regions within each model level, but here we introduce terms representing the exchange of radiation laterally between regions and solve the resulting coupled equations for each layer. This approach may be taken with both the direct incoming shortwave radiation, which is governed by Beer’s law, and the diffuse shortwave and longwave radiation, governed by the two-stream equations. The rate of lateral exchange is determined by the area of cloud “edge”. The validity of the method is demonstrated by comparing with rigorous 3D radiative transfer calculations in the literature for two cloud types in which the 3D effect is strong, specifically cumulus and aircraft contrails. The 3D effect on shortwave cloud radiative forcing varies between around  $-25\%$  and around  $+100\%$ , depending on solar zenith angle. Even with an otherwise very simplistic representation of the cloud, the new scheme exhibits good agreement with the rigorous calculations in both the shortwave and longwave, opening the way for efficient yet accurate representation of this important effect in climate models.

## 1. Introduction

Clouds are a key component of the climate system on account of their strong interaction with radiation (Randall et al., 2007). Numerous studies have highlighted the radiative flux bias in climate models resulting from neglect of sub-grid cloud inhomogeneity (e.g. Cahalan et al., 1994; Pomroy and Illingworth, 2000). Several methods to represent sub-grid inhomogeneity have been proposed that are efficient enough to be included in climate models (Barker, 1996; Pincus et al., 2003; Shonk and Hogan, 2008) and have been used to quantify the impact of cloud horizontal structure and vertical overlap on the global radiation budget (Shonk and Hogan, 2010, 2011).

A related piece of missing physics in the treatment of clouds and radiation in climate models is transport of radiation through cloud sides. In current climate models, radiation is allowed to enter or leave a cloud in a model level only through its base or top. Full 3D radiative transfer calculations have demonstrated that this can lead to substantial errors in cloud radiative forcing, particularly for cumulus clouds (e.g. Pincus et al., 2005), deep convection (DiGiuseppe and Tompkins, 2003), aircraft contrails (Gounou and Hogan, 2007) and cirrus uncinus (Zhong et al., 2008). The magnitude of the 3D effect (the difference in radiative fluxes between radiation calculations including and neglecting 3D transport) is dependent on the ratio of the area of cloud side to the total cloud cover. Therefore cumulus clouds are of particular importance when considering 3D radiative effects: although when present they have a cloud cover of only around 0.25, cumulus regimes cover huge stretches of the tropi-

cal oceans.

The myriad of ways that radiation can interact with a complex cloud field makes it very difficult to devise an accurate yet efficient way to represent 3D effects that is generally applicable. The only method that has been implemented in a general circulation model (GCM) to date is the Tilted Independent Column Approximation (TICA) of Várnai and Davies (1999), which makes the overlap of clouds in different layers more random depending on the solar zenith angle. The resulting increase in total cloud cover is intended to approximately represent the fact that when the sun is near the horizon, incoming solar radiation is more likely to intercept a cloud than when it is overhead. This approach has been implemented in a GCM by Tompkins and DiGiuseppe (2007) and resulted in local changes in top-of-atmosphere net shortwave flux of up to  $200 \text{ W m}^{-2}$ .

Although TICA has the advantage of being conceptually simple and easy to implement in existing radiation schemes, it has several shortcomings. Firstly, it only treats 3D effects associated with *direct* incoming shortwave radiation, not the effects associated with *diffuse* transport of shortwave and longwave radiation, which are not dependent on solar zenith angle. It was shown by Heidinger and Cox (1996) that there is a significant 3D longwave effect for cumulus clouds, and in the next section it will be shown that diffuse transport of shortwave radiation is also important via a mechanism we refer to as *shortwave side escape*.

In this paper we present a new method for representing the interaction of radiation with clouds in GCMs that is able to overcome these difficulties. It uses the familiar division of a

model gridbox into clear and cloudy regions, or in the case of the “Tripleclouds” method of Shonk and Hogan (2008) a split into three regions, two cloudy and one clear. Extra terms are introduced into the equations of radiative transfer that represent the lateral exchange of radiation between regions.

In section 2, a conceptual model of 3D radiative transfer is presented that summarizes the effect of 3D transport by three mechanisms, two in the shortwave and one in both the shortwave and longwave. Results of shortwave 3D radiative transfer calculations from the literature are then presented, which are explained in terms of the first two effects. In sections 3 and 4 we describe how the various parts of a 1D radiative transfer calculation may be modified to include 3D effects. Then in section 5, a simple implementation of the new scheme is used to reproduce the literature results that were shown in section 2.

## 2. Conceptual model

To aid the formulation of the new radiative transfer scheme, it is necessary to build a conceptual model for the ways that 3D effects in the presence of clouds change net fluxes in the longwave and shortwave. This will then be used to explain qualitatively some full 3D radiative transfer calculations in the literature. Figure 1 presents what we consider to be the three dominant mechanisms of 3D radiative transport, adapted from Gounou and Hogan (2007). Várnai and Davies (1999) proposed a more complex model with four separate mechanisms for the shortwave alone, but for the purposes of this paper three mechanisms are sufficient.

The first mechanism, *shortwave side illumination*, is the most widely studied, and is the phenomenon that TICA was designed to address. It increases with solar zenith angle and results in a larger fraction of incoming solar radiation being reflected back to space than in the equivalent calculation using the Independent Column Approximation (ICA) in which no horizontal transport between regions is permitted. The example in Figure 1a shows a case when all of the incoming solar radiation intercepts a cloud, even though the cloud cover is only one third. In the equivalent ICA calculation, two thirds of the incoming radiation would reach the surface without intercepting the cloud (neglecting gaseous scattering and absorption for simplicity).

Figure 2 shows the percentage change to top-of-atmosphere (TOA) shortwave cloud radiative forcing, as a function of solar zenith angle, calculated using full 3D radiative transfer for several different cloud types. Benner and Evans (2001) and Gounou and Hogan (2007) used the Spherical Harmonics Discrete Ordinate Method (SHDOM) of Evans (1998), while Pincus et al. (2005) used a Monte Carlo method. Here, cloud radiative forcing is defined as the difference between the clear-sky and cloudy-sky upwelling shortwave radiation at TOA, i.e.

$$\text{CRF} = F_{\text{clear,TOA}}^+ - F_{\text{cloudy,TOA}}^+ \quad (1)$$

Thus shortwave CRF is negative except over very reflective snow-covered surfaces. The quantity shown in Figure 2 is

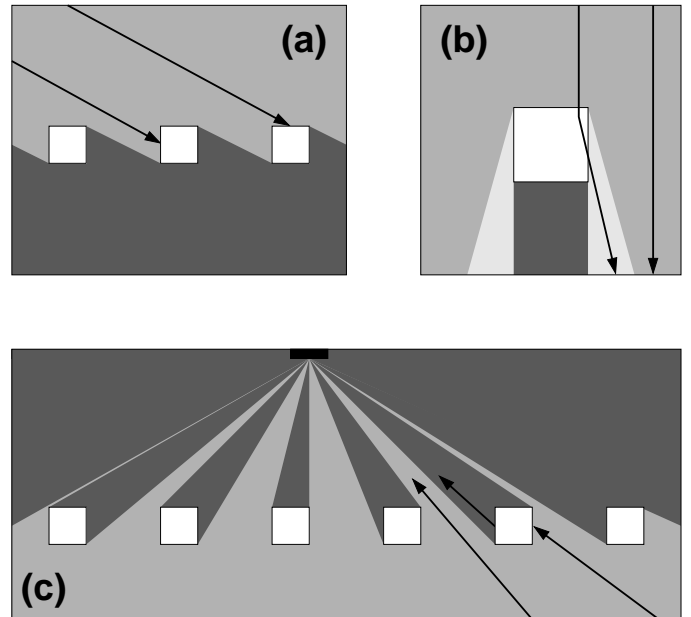


FIG. 1. Schematic explaining how 3D radiative transfer affects cloud radiative forcing (CRF), with the lighter colours outside clouds indicating more intense radiation and the darker colours less intense radiation. *Shortwave side illumination* (a): at high solar zenith angles a greater fraction of incoming solar radiation is intercepted by cloud than in the independent column approximation (ICA), increasing the CRF. *Shortwave side escape* (b): at low solar zenith angles the radiation that escapes out of cloud sides tends to be forward scattered towards the ground, decreasing the CRF. *Shortwave and longwave side exchange* (c): above a field of clouds, the clouds subtend a greater fraction of the downward-looking hemisphere (accounting for  $\cos(\theta)$  dependence of their contribution to the upwelling irradiance) than the areal cloud coverage. Hence the longwave CRF is larger than in the ICA. In the shortwave, less reflected radiation from the surface is able to escape back to space.

given by  $100 \times (\text{CRF}_{3\text{D}} - \text{CRF}_{\text{ICA}}) / \text{CRF}_{\text{ICA}}$ , where  $\text{CRF}_{3\text{D}}$  is the CRF calculated using a full 3D radiative transfer model, while  $\text{CRF}_{\text{ICA}}$  is the CRF calculated using the Independent Column Approximation.

It can be seen in Figure 2 that, for cumulus with a solar zenith angle greater than around  $45^\circ$ , the magnitude of the CRF is increased significantly due to the mechanism of shortwave side illumination. For solar zenith angles greater than around  $80^\circ$ , the calculations of Pincus et al. (2005) for cumulus clouds predict that the magnitude of CRF can be doubled. The results of Gounou and Hogan (2007) for aircraft contrails confirm that side illumination is responsible: when they orientated their contrails perpendicular to the sun (the solid grey line in Figure 2), thereby maximizing the solar illumination of the side of the contrail, the 3D effect was maximized, but orientating their contrails parallel to the sun (the dashed grey line in Figure 2), thereby

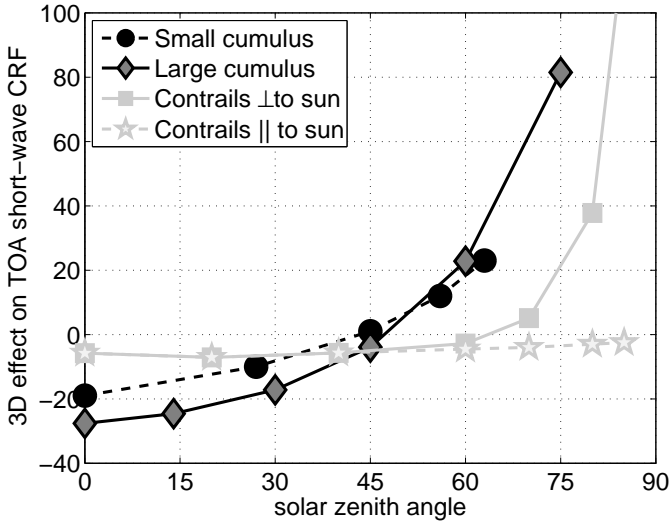


FIG. 2. The effect of 3D radiative transfer on shortwave top-of-atmosphere (TOA) cloud radiative forcing (CRF), versus solar zenith angle, for cumulus clouds and contrails, calculated rigorously using full 3D radiative transfer codes (references given in Table 1).

moving any illumination of the side of the contrail, the CRF enhancement at high solar zenith angles was removed.

It is clear from Figure 2 that side illumination is not the only shortwave 3D effect, since for solar zenith angles less than  $45^\circ$ , the magnitude of the CRF for cumulus and contrails is *reduced* when 3D transport is included, by up to 27% in the study of Pinus et al. (2005). This we explain in Figure 1b by the mechanism of *shortwave side escape*. Shortwave radiation from an overhead sun that enters a cloud through its top may escape from the sides of a cloud, where in the ICA it may not and is more likely to be reflected back to space. Since cloud particles are typically larger than the wavelength of the radiation, the scattering is predominantly in the forward direction, and so radiation escaping from the side of a cloud is more likely to be directed towards the surface than back to space. Therefore, this mechanism reduces CRF relative to an ICA calculation.

In the longwave, inclusion of 3D transport tends to increase the CRF due to the presence of cloud sides, making the cloud a more effective emitter and absorber, as illustrated in Figure 1c and which we refer to as *longwave side exchange*. Essentially the same mechanism was identified by Killen and Ellingson (1994). It was estimated by Heidinger and Cox (1996) that 3D transport in cumulus clouds increases the surface longwave forcing by as much as 30%. Gounou and Hogan (2007) reported that 3D transport typically increases the TOA longwave forcing of contrails by around 10%. There is a large degree of cancellation between the shortwave and longwave CRFs of contrails (Stuber et al., 2006), and therefore it turns out that the modest effects of 3D transport in the shortwave and longwave individually

add up to very substantial effect on net CRF, leading to a doubling or a reversal of the sign depending on solar zenith angle (Gounou and Hogan, 2007). It should be noted that the mechanism in Figure 1c can also modulate the fraction of reflected shortwave radiation from the surface that escapes to space, but the other two mechanisms appear to dominate in the shortwave.

The results reviewed in this section so far have been for clouds with a large area of cloud side relative to their cloud cover, particularly convective clouds such as cumulus. For stratiform clouds the 3D effect is smaller due to the reduced area of cloud side. For example, Zuidema and Evans (1998) reported only around a 2% effect for the interaction of shortwave radiation with stratocumulus clouds. Zhong et al. (2008) found that optically thin cirrus had up to a 15% effect in the shortwave and 10% in the longwave, but reducing for optically thicker ice clouds.

### 3. Method

The top row of Figure 3 presents a schematic of the three steps in a standard 1D radiation scheme. The bottom row presents the equivalent steps in our new scheme that incorporates the effects of 3D transport, which involves modifications to the three existing steps and three additional steps. These procedures are described in full in the following subsections. Section 3a describes how the treatment of the direct incoming shortwave beam may be modified to include radiation exchange between regions. In the shortwave, scattering from the direct beam then acts as a source for the calculation of the diffuse radiation field, while in the longwave, the source for the diffuse radiation field is thermal emission. Section 3b describes how the distribution of sources with height in a single atmospheric layer can be used to calculate the exitant fluxes at the top and bottom of the layer; transport through cloud sides is represented via a two-stage process illustrated by Figures 3e and 3f. Finally, section 3c describes how the sources at layer edges, together with the reflectance and transmittance of each layer, may be used with a discretized version of the two-stream equations to calculate the vertical distribution of upwelling and downwelling diffuse fluxes in the atmosphere. Again, to represent transport through cloud sides, a three-stage process is employed as illustrated in Figures 3g, 3h and 3i.

The equations presented in this section are all monochromatic in the sense that they are valid over a part of the spectrum narrow enough that the scattering and absorption properties of the atmosphere can be considered constant. For simplicity, however, the dependence of each term on wavelength has not been written.

#### a. Direct solar beam

The first step of a 1D radiation calculation in the shortwave part of the spectrum is to determine how much of the *direct* (i.e. unscattered) beam penetrates down to any point in the atmosphere. In the independent column approximation, this calcula-

TABLE 1. Values of cloud fraction  $c_b$ , vertical-to-horizontal aspect ratio  $r$ , optical depth  $\delta$  and single-scatter albedo  $\omega$  from the studies simulated in Figure 2.

Reference	Cloud type	$c_b$	$r$	$\delta$	$\omega$
Benner and Evans (2001)	small cumulus	0.10	0.4	4.4	0.999
Pincus et al. (2005)	large cumulus	0.22	0.7	15	0.999
Gounou and Hogan (2007)	contrails $\perp$ to sun	0.05	0.5	0.4	0.999
Gounou and Hogan (2007)	contrails $\parallel$ to sun	0.05	0.5	0.4	0.999

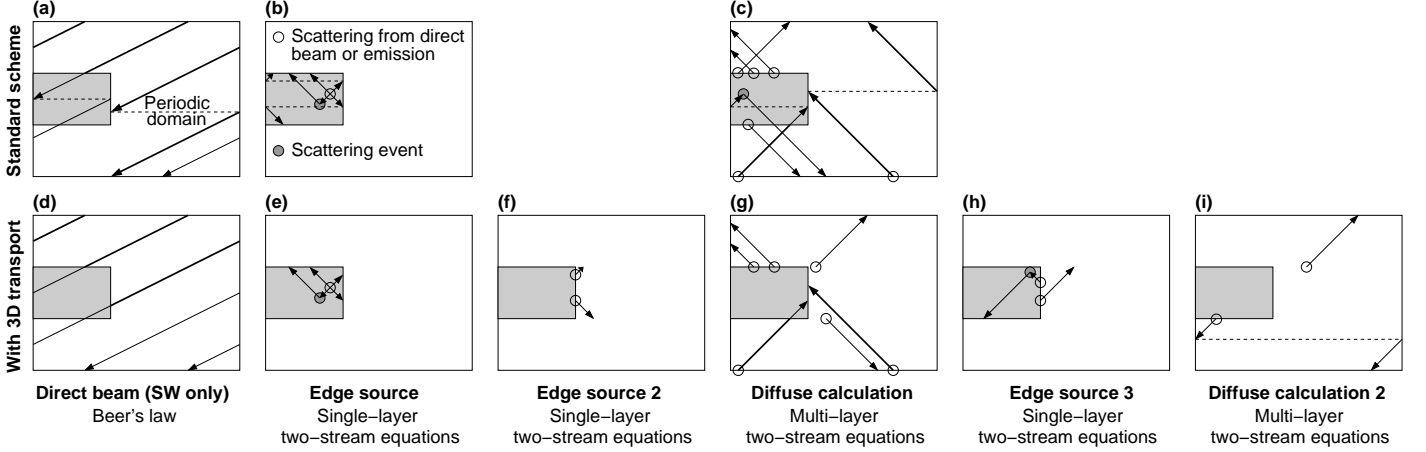


FIG. 3. Schematic showing the various steps in a 1D radiation scheme. The top row shows the three steps in a standard 1D scheme: (a) calculation of the penetration of the direct solar beam to various levels in the atmosphere, (b) the use of this to calculate the upwelling and downwelling radiation sources at layer edges, and (c) the use of surface and edge sources to calculate the profile of diffuse upwelling and downwelling fluxes. In each case, radiation within a particular region (clear or cloudy) is not permitted to travel laterally to the other region; rather the regions are treated as periodic and the implicit transport from one side of a region to the other is illustrated by the dashed horizontal lines. The bottom row shows the equivalent steps in our new scheme, including three additional steps, as described in detail in section 3. The open circles in this figure are used to denote radiation originating from a previous step in the sequence, or in the case of panels (b) and (e) in the longwave, thermal emission.

tion is straightforward: we have to solve

$$\frac{dF}{d\delta} = -\frac{F}{\mu_0}, \quad (2)$$

where  $F(\delta)$  is the direct solar irradiance at a particular point in the atmosphere,  $\delta$  is the zenith optical depth of the atmosphere from the top of the atmosphere down to that point and  $\mu_0$  is cosine of the solar zenith angle. Note that the optical depth and other single-scattering properties refer to delta-Eddington-scaled quantities (Joseph et al., 1976). The solution of (2) is Beer's law, given by

$$F = F_0 \exp\left(-\frac{\delta}{\mu_0}\right), \quad (3)$$

where  $F_0$  is the TOA solar irradiance into a plane that is parallel to the surface of the earth at the wavelength under consideration. In the case that the atmosphere is divided into discrete layers, within which there are multiple regions (e.g. clear and cloudy), we proceed down through the atmosphere from TOA. In a given layer, Beer's law is applied separately to each region

within it, and overlap rules are used to determine how the extant irradiances at the base of that layer are combined to obtain the input irradiances at the top of the regions of the next layer. At the surface, a Lambertian reflector would be represented by treating all of the direct beam that is reflected by the surface as a boundary source term for the diffuse radiation calculation using the two-stream equations (see section 3c).

So how can we account for the direct beam of the sun passing through the sides of clouds? We need to modify (2) for each region to account for lateral exchange of radiation between regions. Since the optical depth of each region will be different, it is necessary to define a common vertical co-ordinate. We use a height co-ordinate,  $z$ , that increases with depth downwards into the layer from zero at the top to  $z_1$  at the base. Thus for two regions  $a$  and  $b$ , we require the corresponding irradiances  $F^a(z)$  and  $F^b(z)$  to satisfy

$$\begin{aligned} \frac{dF^a}{dz} &= -\frac{\beta_e^a}{\mu_0} F^a - f_{\text{dir}}^{ab} F^a + f_{\text{dir}}^{ba} F^b; \\ \frac{dF^b}{dz} &= -\frac{\beta_e^b}{\mu_0} F^b - f_{\text{dir}}^{ba} F^b + f_{\text{dir}}^{ab} F^a, \end{aligned} \quad (4)$$

where  $\beta_e^a$  and  $\beta_e^b$  are the volume extinction coefficients of the two regions of the layer,  $f_{\text{dir}}^{ab}$  represents the rate at which radiation is laterally transported from region  $a$  to region  $b$ , and conversely for  $f_{\text{dir}}^{ba}$ . To avoid breaking the flow of the discussion, we postpone the description of the derivation of these rates until section 4. It is important to define  $F^a$  and  $F^b$  (which have the units  $\text{W m}^{-2}$ ) as the radiative power in a particular region *divided by the area of the entire gridbox* (all regions). This ensures that energy is conserved when the same rate  $f_{\text{dir}}^{ab}F^a$  is used for the power leaving region  $a$  as the power entering region  $b$ . It also means that the mean irradiance of the entire gridbox is simply  $F = F^a + F^b$ . In writing (4) we are assuming that, at any height in the layer, the radiation in a particular region is evenly distributed across it, so that the rate of escape to another region is simply proportional to the mean irradiance in the region.

Equation 4 may be solved as a pair of coupled ordinary differential equations (ODEs) assuming that the incoming irradiances at the top of the layer,  $F^a(0)$  and  $F^b(0)$ , are known. The solution is:

$$\begin{aligned} F^a(z) &= \frac{(q+a-b)F^a(0) - 2f_{\text{dir}}^{ba}F^b(0)}{2q} \exp(k_1 z) \\ &+ \frac{(q-a+b)F^a(0) + 2f_{\text{dir}}^{ba}F^b(0)}{2q} \exp(k_2 z); \\ F^b(z) &= \frac{(q-a+b)F^b(0) - 2f_{\text{dir}}^{ab}F^a(0)}{2q} \exp(k_1 z) \\ &+ \frac{(q+a-b)F^b(0) + 2f_{\text{dir}}^{ab}F^a(0)}{2q} \exp(k_2 z), \end{aligned} \quad (5)$$

where

$$a = \beta_e^a / \mu_0 + f_{\text{dir}}^{ab}; \quad (6)$$

$$b = \beta_e^b / \mu_0 + f_{\text{dir}}^{ba}; \quad (7)$$

$$q = \left( a^2 + b^2 - 2ab + 4f_{\text{dir}}^{ab}f_{\text{dir}}^{ba} \right)^{1/2}; \quad (8)$$

$$k_1 = -(a+b+q)/2; \quad (9)$$

$$k_2 = -(a+b-q)/2. \quad (10)$$

It can be shown by substitution that in the case of zero lateral transport between regions ( $f_{\text{dir}}^{ab} = f_{\text{dir}}^{ba} = 0$ ), the solutions given by (5) reduce to Beer's law for the two regions separately.

Figure 4 compares the profile of direct fluxes in clear and cloudy regions for a case with a cloud cover of 1/3 and a solar zenith angle of  $80^\circ$ . The dashed lines correspond to a standard 1D radiation scheme in which transport between regions is neglected and it can be seen that the almost all of the radiation incident at the top of the clear-sky region reaches the base, while virtually none reaches the base of the cloudy region. In contrast, the solid lines include the effect of transport between regions described by (5). Here it can be seen that more than half of the radiation that enters the top of the clear-sky region passes through the side of the cloud before reaching the base of the clear-sky region, resulting in a non-negligible amount of direct-beam radiation in the cloudy region at all heights.

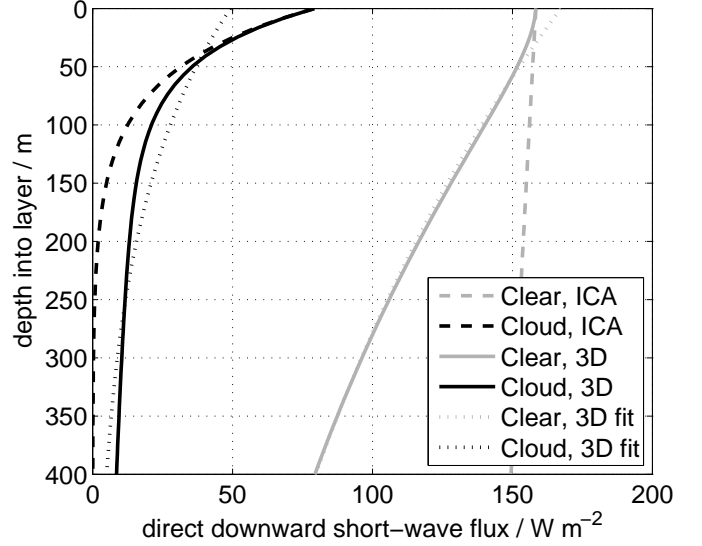


FIG. 4. Simulation of the effect of lateral transport on the direct downwelling shortwave irradiance  $F$  in a layer, versus the depth into the layer  $z$ . The layer contains two regions: a cloud with cloud fraction 1/3, optical depth 5 (before delta-Eddington scaling), asymmetry factor 0.85 and vertical-to-horizontal aspect ratio unity; and a clear-sky region with an optical depth of 0.01. The solar zenith angle is  $80^\circ$ , and the irradiances entering the top of the clear and cloudy regions are in proportion to their areal coverage. The dashed lines show the profiles for the clear and cloudy regions in the independent column approximation, each obeying Beer's law. The solid lines show the same but with lateral transport modelled by (5). The dotted line shows the single-exponential fit to the two-exponential solution, required in section 3b.

To determine the irradiances at the base of regions  $a$  and  $b$  of the layer, we substitute  $z = z_1$  into (5). As before, overlap rules are then used to determine how the irradiances are combined to find the inputs at the top of the next layer down in the atmosphere. It can be seen in Figure 4 that there is a considerable reduction of order 40% in the total direct flux reaching the base of the layer, as would be expected from the conceptual model of shortwave side illumination presented in Figure 1a.

This may be extended to treat more than two regions, such as the Tripleclouds scheme of Shonk and Hogan (2008), where horizontally inhomogeneous clouds are treated as two internally homogeneous regions (in addition to the clear-sky region) with different optical depths. In this case, (4) would be extended to include an extra equation for the irradiance in the third region  $F^c(z)$ , and additional terms would be added to each of the three equations to represent the gain to or loss from region  $c$ . In this case the solution for two regions presented in (5)–(10) would be replaced by the solution for three regions.

*b. Diffuse edge sources*

To describe the transport of the *diffuse* component of the radiation field, the two-stream equations are employed. They treat the radiation into the upward and downward hemispheres as a pair of discrete irradiances  $G^+$  and  $G^-$ , travelling in directions  $+\mu_1$  and  $-\mu_1$ , respectively. Values for  $\mu_1$  vary between radiation schemes, but a typical value is 0.6 (Fu et al., 1997), corresponding to a zenith angle  $\theta_1$  of  $53^\circ$ . The first part is applied independently in each layer to work out how much of the source in the interior of the layer emerges from the top and bottom of that layer. These ‘‘edge sources’’ are then used in the second two-stream step described in section 3c.

In the familiar 1D case with lateral transport between regions, the two-stream equations form a pair of coupled ordinary differential equations (ODEs) that may be applied separately within each region of a given layer of the atmosphere. To represent 3D effects, we may apply the same procedure as for the direct beam, and add lateral transport terms, such that the two-stream equations become

$$\begin{aligned} \frac{dG^{a-}}{dz} &= \beta_e^a (-\gamma_1^a G^{a-} + \gamma_2^a G^{a+} + S_F^{a-}) \\ &\quad - f_{\text{diff}}^{ab} G^{a-} + f_{\text{diff}}^{ba} G^{b-}; \\ -\frac{dG^{a+}}{dz} &= \beta_e^a (-\gamma_1^a G^{a+} + \gamma_2^a G^{a-} + S_F^{a+}) \\ &\quad - f_{\text{diff}}^{ab} G^{a+} + f_{\text{diff}}^{ba} G^{b+}, \end{aligned} \quad (11)$$

and similarly for region  $b$ . Other regions may be added by including further terms for the exchange between them. Within the brackets on the right-hand side, the three terms are as in the standard two-stream equations, representing respectively the loss by scattering and absorption (except for radiation that is scattered but remains within the same hemisphere), gain by scattering from the other direction, and internal sources (i.e. scattering from the direct beam in the shortwave and thermal emission in the longwave). Scattering and absorption are governed by the coefficients  $\gamma_1$  and  $\gamma_2$ , given by

$$\gamma_1 = \frac{1}{\mu_1} \left[ 1 - \frac{\omega(1+g)}{2} \right]; \quad (12)$$

$$\gamma_2 = \frac{1}{\mu_1} \left[ \frac{\omega(1-g)}{2} \right], \quad (13)$$

where  $\omega$  and  $g$  are the single scattering albedo and asymmetry factor of the medium. Note that other formulations for these terms have been proposed in the literature (Meador and Weaver, 1980). The final two terms of (11) represent lateral transport between regions, governed by transfer coefficients  $f_{\text{diff}}^{ab}$  and  $f_{\text{diff}}^{ba}$ , which we define in section 4.

We now discuss the source terms  $S_F^\pm(z)$ . In the case of longwave radiation, thermal emission is isotropic and so  $S_F^+ = S_F^- = B[T(z)]$ , where  $B$  is the Planck function at temperature  $T$  in the wavelength interval being simulated. In the case of shortwave radiation,  $S_F^\pm$  represents scattering from the direct solar beam.

The rate of extinction of the direct beam in (4) is  $(\beta_e/\mu_0)F$ , a fraction  $\omega$  of which is scattered rather than being absorbed. Therefore, the source terms are given by

$$S_F^+ = \frac{\omega\gamma_3}{\mu_0} F; \quad (14)$$

$$S_F^- = \frac{\omega(1-\gamma_3)}{\mu_0} F, \quad (15)$$

where  $\gamma_3$  represents the fraction of scattered direct solar radiation that enters the upward hemisphere, and is given by

$$\gamma_3 = \frac{1-3g\mu_0\mu_1}{2}, \quad (16)$$

according to Liou (1980).

In principle, the solution obtained for the direct solar irradiances  $F$  in (5) could be converted to sources via (14) and (15) and substituted directly into (11), and similarly for region  $b$ . However, the fact that (5) describes  $F$  in terms of two exponentials means that the formal solution to this system has an excessively large number of terms. Therefore, we first fit a single exponential to the two exponentials using the technique given in the appendix, thus assuming that the source terms  $S_F^\pm$  can be represented as varying exponentially with  $z$  as

$$S_F^{a+} = S_0^{a+} \exp(s_{a+}z), \quad (17)$$

and similarly for the other source terms. The coefficients  $S_0^{a+}$  and  $s_{a+}$  are the result of the fitting procedure. The dotted lines in Figure 4 demonstrate the fact that this is usually a reasonable approximation. In the longwave it is common to assume that the Planck function varies exponentially within a layer (e.g. Fu et al., 1997), so (17) is also applicable in the longwave.

Thus (11) represents four coupled linear ODEs for  $G^{a+}$ ,  $G^{a-}$ ,  $G^{b+}$  and  $G^{b-}$ . This is equivalent to the four-stream discrete ordinate method for radiative transfer (e.g. Thomas and Stamnes, 1999), except that rather than the four streams corresponding to irradiances in four different directions, our four streams correspond to irradiances in two directions and in two adjacent regions. However, we cannot simply apply an existing four-stream solution to the two-stream-two-region problem, because the latter lacks some of the symmetries of the former. For example, in a four-stream scheme, the rate at which radiation is scattered from stream 1 to stream 2 is equal to the rate at which radiation is scattered from stream 2 to stream 1. This symmetry does not apply if the two streams are in different regions and the regions are of different size (i.e. the cloud fraction is not equal to one half), because then the rate at which radiation in the upwelling stream of the smaller region is transported into the upwelling stream of the larger region is greater than the rate of migration back into the smaller region. According to Thomas and Stamnes (1999), this symmetry breaking would result in a factor of eight increase in computational time.

A key consideration is that, in practice, the two regions are only weakly coupled. An individual photon may be scattered

between the upwelling and downwelling hemispheres several times before exiting a layer, but it is much less likely to be exchanged laterally between regions more than once before exiting the layer through the base or the top. This enables the four coupled equations represented by (11) (and the equivalent equations for  $G^{b\pm}$ ) to be replaced by two pairs of coupled equations that are solved independently in a two-step process illustrated by Figures 3e and 3f. In the first step, the source terms in (11) representing transport from the other region are removed while the sink term that is due to lateral transport out of the region is retained, yielding

$$\begin{aligned}\frac{dG^{a-}}{dz} &= \beta_e^a (-\hat{\gamma}_1^a G^{a-} + \gamma_2^a G^{a+} + S_F^{a-}); \\ -\frac{dG^{a+}}{dz} &= \beta_e^a (-\hat{\gamma}_1^a G^{a+} + \gamma_2^a G^{a-} + S_F^{a+}),\end{aligned}\quad (18)$$

where we have incorporated this sink into an “effective  $\gamma_1$ ”, of the form

$$\hat{\gamma}_1^a = \gamma_1^a + f_{\text{diff}}^{ab} / \beta_e^a. \quad (19)$$

A similar pair of equations may be written for region  $b$ . In this step we are treating radiation that escapes through cloud sides to be lost to the system, to be picked up only in the second step.

The equations in (18) are in the same two-stream form as considered by Thomas and Stamnes (1999) and Fu et al. (1997). Therefore we may apply the same solution to obtain the exitant fluxes at the top and bottom of the layer that are due to the sources  $S_F^{a\pm}$ . Neglecting the superscript  $a$  for brevity, the solution for  $G^\pm$  has the form

$$\begin{aligned}G^+(z) &= g_1 t \exp(kz) + g_2 r \exp(-kz) + Z^+(z); \\ G^-(z) &= g_1 r t \exp(kz) + g_2 \exp(-kz) + Z^-(z),\end{aligned}\quad (20)$$

where the first two terms on the right-hand side represent the solution to the homogeneous part of (18) (i.e. with the sources set to zero), where

$$k = \beta_e (\hat{\gamma}_1^2 - \gamma_2^2)^{1/2}; \quad (21)$$

$$r = \frac{\beta_e \hat{\gamma}_1 - k}{\beta_e \gamma_2} = \frac{\beta_e \gamma_2}{\beta_e \hat{\gamma}_1 + k}; \quad (22)$$

$$t = \exp(-kz_1), \quad (23)$$

while  $Z^\pm$  is the particular solution, related to the inhomogeneous part of (18) (the source terms), and is given by

$$\begin{aligned}Z^+(z) &= \beta_e \left( \frac{s_+ + \beta_e \hat{\gamma}_1}{k^2 - s_+^2} S_F^+(z) + \frac{\beta_e \gamma_2}{k^2 - s_-^2} S_F^-(z) \right); \\ Z^-(z) &= \beta_e \left( \frac{\beta_e \hat{\gamma}_1 - s_-}{k^2 - s_-^2} S_F^-(z) + \frac{\beta_e \gamma_2}{k^2 - s_+^2} S_F^+(z) \right),\end{aligned}\quad (24)$$

and the  $s_\pm$  terms describe the height distribution of the upwelling and downwelling source following (17). The coefficients  $g_1$  and  $g_2$  may be determined from boundary conditions, i.e. by substituting zero for the downwelling irradiance at the

top of the layer,  $G^-(0)$ , and the upwelling irradiance at the base of the layer,  $G^+(z_1)$ . This yields

$$\begin{aligned}g_1 &= \frac{Z^+(z_1) - rtZ^-(0)}{r^2 t^2 - 1}; \\ g_2 &= \frac{Z^-(0) - rtZ^+(z_1)}{r^2 t^2 - 1},\end{aligned}\quad (25)$$

where the  $Z^\pm(0)$  and  $Z^\pm(z_1)$  terms are found by substituting the known source terms given by (17) into (24) at the top and bottom of the layer, respectively.

Thus we derive the exitant irradiance at the top and base of region  $a$  and layer  $i$ , due solely to the sources within that region, as

$$\begin{aligned}\Sigma_{G,i}^{a+} = G^{a+}(0) &= Z^+(0) \\ &+ \frac{Z^+(z_1)(1-r^2)t + Z^-(0)(1-t^2)r}{r^2 t^2 - 1}; \\ \Sigma_{G,i}^{a-} = G^{a-}(z_1) &= Z^-(z_1) \\ &+ \frac{Z^+(z_1)(1-t^2)r + Z^-(0)(1-r^2)t}{r^2 t^2 - 1}.\end{aligned}\quad (26)$$

We use the notation  $\Sigma$  for the edge sources to avoid confusion with the continuous source distribution  $S$  described previously. The arrows reaching the top of the cloudy region in Figure 3e display schematically the component of the radiation field represented by  $\Sigma_{G,\text{top}}^{a+}$  above.

The extra step to represent 3D transport, depicted in Figure 3f, is to calculate what happens to the radiation that escaped through the cloud sides. We perform a second diffuse source calculation, but this time using the radiation entering region  $b$  from region  $a$  as the source function and setting the lateral radiation transfer rates to zero, as no further transfer is allowed in this second step. As the distribution of diffuse radiation through each region is different in this second step, we use the notation  $H^\pm$  in place of  $G^\pm$ . This gives

$$\begin{aligned}\frac{dH^{a-}}{dz} &= \beta_e^a (-\gamma_1^a H^{a-} + \gamma_2^a H^{a+} + S_G^{a-}); \\ -\frac{dH^{a+}}{dz} &= \beta_e^a (-\gamma_1^a H^{a+} + \gamma_2^a H^{a-} + S_G^{a+}),\end{aligned}\quad (27)$$

where the sources are

$$\begin{aligned}S_G^{a-}(z) &= \frac{f_{\text{diff}}^{ba}}{\beta_e^a} G^{b-}(z); \\ S_G^{a+}(z) &= \frac{f_{\text{diff}}^{ba}}{\beta_e^a} G^{b+}(z).\end{aligned}\quad (28)$$

Similar equations can be written to account for the  $S_G^{b\pm}$  sources.

Note that the form of (27) is the same as (18), but is the equivalent 1D calculation (depicted in Figure 3b). The difference is the application of  $\gamma_1$  in place of  $\hat{\gamma}_1$ . When (24) is substituted into (20), we find that  $G^{a+}$ ,  $G^{a-}$ ,  $G^{b+}$  and  $G^{b-}$  are each

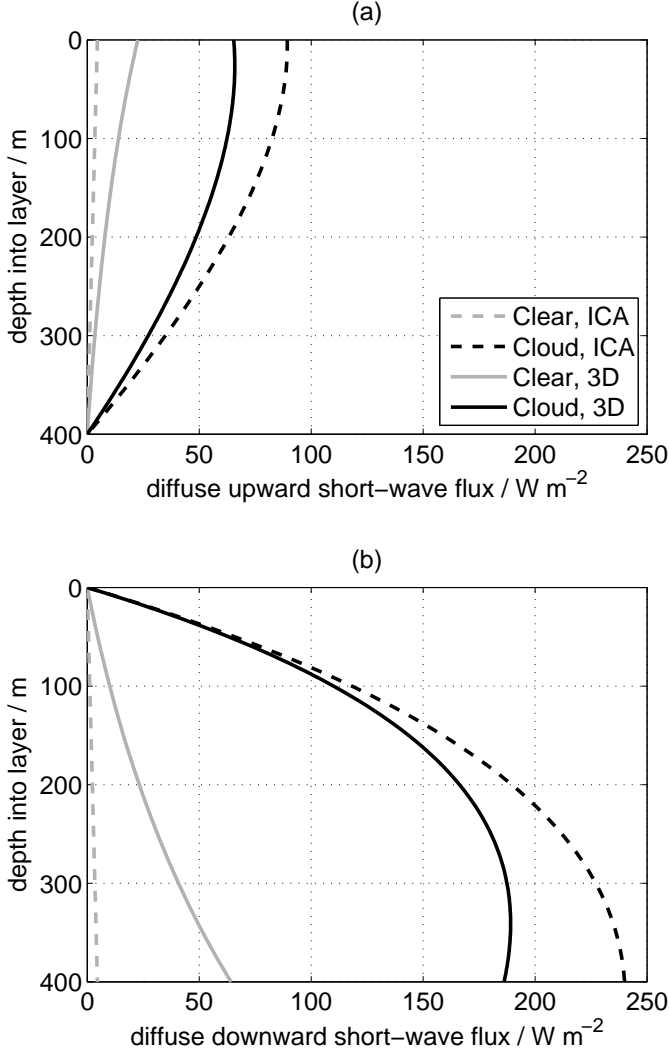


FIG. 5. Simulation of the effect of lateral transport on the diffuse shortwave flux  $F$  within a layer, versus the physical depth into the layer  $z$ . The diffuse fluxes are calculated from sources solely within the layer. The layer contains two regions: a cloud with cloud fraction 1/3, and the same properties as in Figure 4. The dashed lines show the profiles for the clear and cloudy regions in the independent column approximation; the solid lines show the same but with lateral transport included using the modified equations in section 3b.

represented by the sum of four exponentials. The method in the appendix is used again to approximate them by a single exponential. We can then solve (27) using exactly the same method as in the first step, but with  $\gamma_1$  substituted in place of  $\hat{\gamma}_1$  to give flux distributions  $H^{a+}$ ,  $H^{a-}$ ,  $H^{b+}$  and  $H^{b-}$ . This gives a second set of edge sources ( $\Sigma_{H,i}^{a+}$ ,  $\Sigma_{H,i}^{a-}$ ,  $\Sigma_{H,i}^{b+}$  and  $\Sigma_{H,i}^{b-}$ ) which can be added respectively to the first set ( $\Sigma_{G,i}^{a+}$ ,  $\Sigma_{G,i}^{a-}$ ,  $\Sigma_{G,i}^{b+}$  and  $\Sigma_{G,i}^{b-}$ ) from (26) to give the total edge sources.

The treatment of 3D radiation in this section can be used to

explain the mechanism of shortwave side escape that was depicted in Figure 1b. Figure 5 shows the same cloud as considered in Figure 4, but this time illuminated by an overhead sun. The distribution of upward and downward diffuse fluxes in each of the regions within a layer that are due to sources in that layer only are shown in panels (a) and (b) respectively. It should be noted that, for the radiation calculation, only the exitant diffuse fluxes at the top and bottom of the layer are required, but we can clearly see the effects of shortwave side escape in both panels. When lateral radiation transport is allowed for an overhead sun, we expect increased amounts of radiation to reach the surface in the clear regions, with a corresponding decrease in radiation reaching the surface in the cloudy region. The dashed lines show the distributions for the ICA calculations; the solid lines show the same for the 3D calculations. Comparison of the two reveals a small 2.5% increase in diffuse flux reaching the bottom of the layer.

### c. Diffuse radiation profile

The final step in the radiative transfer calculation is to use the edge sources calculated in section 3b in a multi-layer implementation of the two-stream equations. The standard approach is to define reflection and transmission functions for each layer and region as follows (Meador and Weaver, 1980):

$$R = \frac{\beta_e \gamma_2 (1 - t^2)}{k + \beta_e \gamma_1 + (k - \beta_e \gamma_1) t^2}; \quad (29)$$

$$T = \frac{2kt}{k + \beta_e \gamma_1 + (k - \beta_e \gamma_1) t^2}, \quad (30)$$

where the terms were defined in (12)–(13) and (21)–(23). Defining the indices of the layers to increase downwards, the upwelling radiative flux at the top of region  $a$  of layer  $i$ ,  $I_{i+1/2}^{a+}$ , is the sum of transmitted flux through the layer, the fraction of the downwelling flux that is reflected back, and the upwelling source from the layer:

$$I_{i+1/2}^{a+} = T_i^a I_{i+1/2}^{a+} + R_i^a I_{i-1/2}^{a-} + \Sigma_i^{a+}, \quad (31)$$

and similarly for region  $b$ . Likewise, the downwelling flux at the base of region  $a$  of layer  $i$  is given by:

$$I_{i+1/2}^{a-} = T_i^a I_{i-1/2}^{a-} + R_i^a I_{i+1/2}^{a+} + \Sigma_i^{a-}, \quad (32)$$

and similarly for region  $b$ . At the surface (mid-level  $n - 1/2$ ), the upwelling flux is given by

$$I_{n-1/2}^{a+} = \alpha_s (I_{n-1/2}^{a-} + F_{n-1/2}^a) + (1 - \alpha_s) B(T_s), \quad (33)$$

where  $\alpha_s$  is the surface albedo,  $F_{n-1/2}^a$  is the direct downwelling solar radiation at the surface (zero in the longwave) and  $B(T_s)$  is the Planck function at surface temperature (assumed to be zero in the shortwave).

In the case of a horizontally homogeneous atmosphere, we have only one region  $a$ , and the equations for the upwelling and

downwelling fluxes at each layer interface may be combined into a tridiagonal system of linear equations that is efficiently solved. When each layer of the atmosphere is divided into two or more regions, with arbitrary overlap between regions in different layers, the system becomes more complicated to solve. It was shown by Shonk and Hogan (2008) that the most obvious approach of writing the equations out as a linear system of equations and solving the matrix problem results in anomalous horizontal radiation transport below cloud base from the sunlit to the shadowed part of the gridbox. This is clearly a serious drawback when we are trying to devise a method to calculate horizontal transport accurately. Shonk and Hogan (2008) presented an efficient method to solve the system of equations that overcomes this problem, which we use as a basis for the extension to include 3D transport.

So how may we modify (31) and (32) to include transport between regions? One approach would be to add extra terms representing gain from and loss to the adjacent region, although this turns out to be excessively complicated, and impossible to incorporate within the Shonk and Hogan (2008) solver. Instead we take a similar approach to section 3b, and assume that in the lifetime of a photon as treated by the multi-layer two-stream equations, it never travels through more than one cloud side. This enables the diffuse calculation to be split into two steps, as illustrated by Figures 3g and 3h. In the first step, we use the Shonk and Hogan (2008) solver, but with an additional sink of radiation representing loss of radiation through cloud sides. This is achieved by using (29) and (30) to calculate  $R$  and  $T$  but with  $\gamma_1$  replaced by  $\hat{\gamma}_1$  as defined in (19), which produces the profile of upwelling and downwelling fluxes due to radiation that has not passed through the side of a cloud (at least, not since its first interception of a layer boundary as discussed in section 3b). The edge source terms in (31) and (32) are set as the sum of the edge sources from the previous two steps; i.e.,  $\Sigma_i^{a\pm} = \Sigma_{G,i}^{a\pm} + \Sigma_{H,i}^{a\pm}$ .

This profile is then used to calculate the source terms for the second step. We describe the upwelling flux in region  $a$  of a layer  $i$ ,  $J_i^{a+}$ , as a function of depth into the layer as the sum of two exponentials:

$$J^{a+}(z) = A_i^{a+} \exp(k_i^{a+} z) + B_i^{a+} \exp(-k_i^{a+} z), \quad (34)$$

where  $k_i^{a+}$  is as defined in (21). Application of boundary conditions

$$J^{a+}(0) = I_{i-1/2}^{a+} - (\Sigma_{I,i}^{a+} + \Sigma_{J,i}^{a+}); \quad (35)$$

$$J^{a+}(z_1) = I_{i+1/2}^{a+} \quad (36)$$

can be used to determine the  $A$  and  $B$  coefficients. Note that we remove all internal sources from the calculation, as it is only the diffuse flux in the layer that originated *from other layers* that we are allowing to transfer regions (the diffuse flux represented by the edge sources originates *from the current layer* and has already been allowed to transfer between regions).

Following the approach encapsulated in (28), we then define the source function for upwelling radiation entering region  $b$  from region  $a$  simply as

$$S_J^{b+}(z) = \frac{f_{\text{diff}}^{ab}}{\beta_e^b} J^{a+}(z), \quad (37)$$

and similarly for the other source terms. We then follow the procedure in the second step of section 3b to calculate a new set of boundary sources  $\Sigma_{H',i}^{\pm}$  in regions  $a$  and  $b$ . These are then used as the sources in a second call of the Shonk and Hogan (2008) solver, except that this time,  $R$  and  $T$  are calculated exactly as in (29) and (30), thereby permitting no further transport between cloud sides. This generates a second profile of upwelling and downwelling fluxes  $I^{\pm}$ , which can then be added to the first profile  $I^{\pm}$  to obtain the full set of diffuse fluxes including 3D radiative transfer. In the shortwave the direct incoming beam versus height would be added to the downwelling diffuse component to obtain the total downwelling flux profile. Section 5 includes an example where all the contributions to the diffuse flux are plotted separately.

#### 4. Lateral radiation transfer rates

The lateral exchange of direct radiation between regions in a given layer is governed by coefficients  $f_{\text{dir}}^{ab}$  and  $f_{\text{dir}}^{ba}$  in (4), while the exchange of diffuse radiation is governed by  $f_{\text{diff}}^{ab}$  and  $f_{\text{diff}}^{ba}$  in (11). In this section, we derive expressions for these coefficients. To achieve this, we assume that the clouds are vertically uniform within a model level, and hence that the cloud edges are perfectly vertical surfaces. The extent to which this is a valid assumption was explored by Brooks et al. (2005).

##### a. Direct radiation: general considerations

We first estimate the rate at which direct radiation from the sun with solar zenith angle  $\theta_0$  will enter through the side of a cloud. Consider an infinitesimally thin layer of depth  $dz$  within a gridbox that has a horizontal area of  $A$ . The gridbox contains a clear-sky region of area  $A_a$  and a cloudy region of area  $A_b$  such that  $A = A_a + A_b$ . Figure 6a shows a plan view of the distribution of cloud in the gridbox, where the area  $dA$  indicates the region of clear sky where sunlight entering at the top of the thin layer  $dz$  (with the sun to the right of the scene in this case) would enter the cloud edge before reaching the bottom of this layer. As we assume incident radiation into the top of the layer to be uniformly distributed over each separate region, the change in direct flux in region  $a$  due to lateral transport to region  $b$ ,  $dF^a$ , is governed by

$$\frac{dF^a}{F^a} = -\frac{dA}{A_a}. \quad (38)$$

The negative sign is because  $F^a$  is reduced with increasing depth into the layer by this transport. To calculate  $dA$  we consider the geometry of what happens at the cloud edge, depicted in plan and side views in Figures 6d and 6e. From Figure 6d, we can

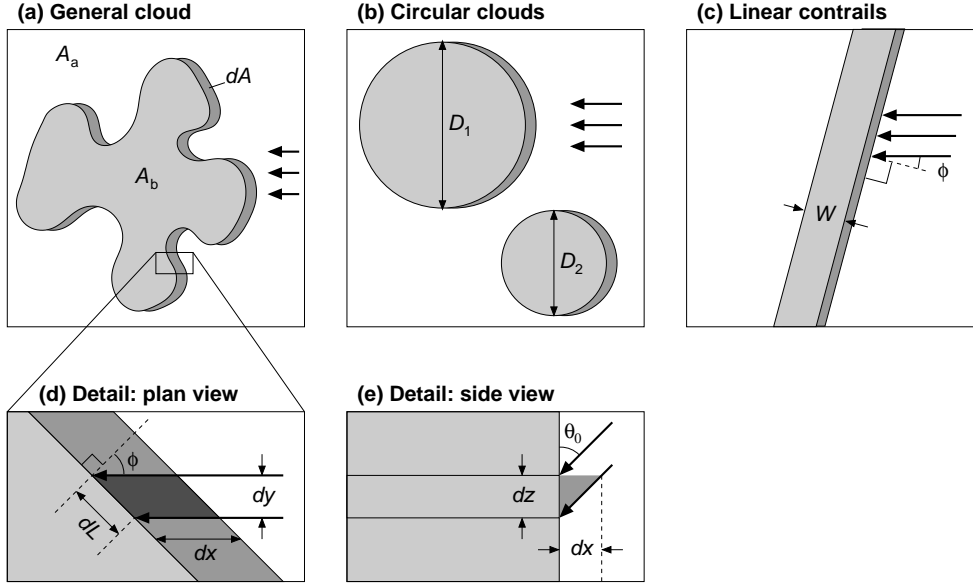


FIG. 6. Schematic illustrating how the rate at which direct-beam solar radiation enters the sides of clouds is calculated. Panel (a) shows a plan view of a general cloud field in which there is no preferred orientation of the cloud edge with respect to the sun. The area  $dA$  indicates where solar radiation (from above and to the right as indicated by the thick arrows) incident on a thin layer of thickness  $dz$  would enter the cloud from the side. Panels (b) and (c) depict particular cloud distributions, one with circular clouds and the other with a linear contrail. Panels (d) and (e) depict magnified views of the cloud edge from above and the side, respectively, from which the area  $dA$  may be calculated.

see that  $dA$  may be given by

$$dA = dx \int_L dy, \quad (39)$$

where  $dx$  is the width of infinitesimal area  $dA$  in the direction of the sun, and from Figure 6e we have that  $dx = \tan(\theta_0) dz$ . The integration is performed over the entire length of cloud edge  $L$  in the gridbox, and  $dy$  is the length projected towards the sun by a small piece of cloud edge of length  $dL$ . From Figure 6d we see that  $dy = H(\pi/2 - |\phi|) \cos(\phi) dL$ , where  $\phi$  is the angle that the normal to the cloud edge makes to the sun. Here,  $H(x)$  is the Heaviside function (equal to 1 for  $x > 0$  and 0 otherwise) and ensures that we only consider cloud edges that are sunlit, i.e. those for which  $|\phi| < \pi/2$ . The integral will depend on the particular cloud geometry in question, and will shortly be evaluated for particular cloud configurations, but we expect that, on average, the length of cloud edge for a given type of scene will increase in proportion to the gridbox area. Therefore it makes sense to define the *effective length of cloud edge projected towards the sun per unit area* as a resolution-independent property of any cloud distribution, given by

$$\begin{aligned} L_{\text{dir}}^{ab} &= \frac{1}{A} \int_L dy \\ &= \frac{1}{A} \int_L H(\pi/2 - |\phi|) \cos(\phi) dL \\ &= \frac{L}{A} \int_{-\pi}^{\pi} p(\phi) H(\pi/2 - |\phi|) \cos(\phi) d\phi. \end{aligned} \quad (40)$$

The final form in (40) replaces the integration along the total length of cloud edge in the gridbox  $L$  with an integration over  $\phi$ , where  $p(\phi)$  is the probability density of  $\phi$ . Substitution of (39) and (40) into the first form of (38) and rearranging gives

$$-\frac{1}{F^a} \frac{dF^a}{dz} \Big|_{ab} = \frac{AL_{\text{dir}}^{ab} \tan(\theta_0)}{A_a}, \quad (41)$$

where we have clarified that the derivative is only the part of the total derivative that is due to loss by transport from region  $a$  to region  $b$ . It can be seen from (4) that the left hand side of (41) is simply the definition  $f_{\text{dir}}^{ab}$ . By defining the clear-sky fraction as  $c_a = A_a/A$ , we obtain

$$f_{\text{dir}}^{ab} = L_{\text{dir}}^{ab} \tan(\theta_0) / c_a. \quad (42)$$

The same procedure may be used to derive the rate of transport between regions  $b$  and  $a$  as  $f_{\text{dir}}^{ba} = L_{\text{dir}}^{ba} \tan(\theta_0) / c_b$ , but on average for plausible cloud fields the length of cloud edge oriented toward the sun is equal to the length of cloud edge oriented away from the sun (the latter being associated with direct radiation escaping from region  $b$  to region  $a$ ), so we have the result that  $L_{\text{dir}}^{ba} = L_{\text{dir}}^{ab}$ .

#### b. Direct radiation: specific cases

We now have the task of defining  $L_{\text{dir}}^{ab}$  for particular cloud types and geometries. We first consider the situation in most natural cloud fields where there is no preferred orientation of

the sun with respect to the cloud edge, which means that the angle  $\phi$  in Figure 6d is uniformly distributed between  $-\pi$  and  $+\pi$ , i.e.  $p(\phi) = 1/(2\pi)$  in (40). Hence (40) becomes

$$L_{\text{dir}}^{ab} = \frac{L}{2\pi A} \int_{-\pi/2}^{\pi/2} \cos(\phi) d\phi = \frac{L}{\pi A}. \quad (43)$$

If we have a particular 3D cloud field for which we wish to perform a radiation calculation including 3D transport using the technique developed in this paper, then it is straightforward to compute the total cloud perimeter  $L$  at each height and hence  $L_{\text{dir}}^{ab}$  and  $f_{\text{dir}}^{ab}$ .

In a general circulation model, however,  $L$  will need to be parameterized. It is convenient to consider the idealized case of cumulus-like clouds with a circular cross-section as illustrated in Figure 6b. If a gridbox contains  $n$  clouds of mean diameter  $\bar{D}$  then the effective length of cloud edge projected towards the sun per unit area is  $L_{\text{dir}}^{ab} = n\bar{D}/A$  while the cloud fraction is  $c_b = (1/A) \sum_i^n \pi(D_i/2)^2 = n\pi\bar{D}^2/(4A)$ . Eliminating  $n/A$  we obtain

$$L_{\text{dir}}^{ab} = \frac{4}{\pi} \frac{c_b}{D_{\text{eff}}}, \quad (44)$$

where the *effective cloud diameter* is  $D_{\text{eff}} = \overline{D^2}/\bar{D}$ . Combining (43) and (44) we obtain  $D_{\text{eff}} = 4c_b A/L$ , which indicates that  $D_{\text{eff}}$  may be derived as a convenient lengthscale from any cloud field without imposing the assumption of circular clouds. In fact, this is exactly the same definition of effective cloud diameter considered by Jensen et al. (2008) in their analysis of satellite data, so statistics on the values of  $D_{\text{eff}}$  are already available for different cloud fields. A similar quantity has also been derived from cloud-resolving models (Neggers et al., 2003). Some convection schemes (e.g. Bechtold et al., 2001) make an explicit assumption about updraught diameter, although evaluation against observations would be needed to test whether this is sufficiently similar to the cloud diameter to be used in the radiation scheme.

Linear contrails constitute another specific cloud configuration to be considered; Figure 6c depicts a contrail with width  $W$  whose normal makes an angle  $\phi$  with the sun. If a model gridbox contains a length  $X$  of contrail then the cloud fraction will be  $c_b = XW/A$  and the total length of cloud edge will be  $L = 2X$ . In this case, the integral in (40) simplifies to  $(1/2) \cos(\phi)$  (where now  $\phi$  is the angle that the normal to the contrail makes to the sun) and

$$L_{\text{dir}}^{ab} = \frac{2X}{A} \frac{\cos(\phi)}{2} = \frac{c_b \cos(\phi)}{W}. \quad (45)$$

### c. Diffuse radiation

The lateral transfer rates of diffuse radiation  $f_{\text{diff}}^{ab}$  and  $f_{\text{diff}}^{ba}$  can be calculated using the same method as for direct radiation. The differences are that in a typical two-stream scheme the radiation is assumed to be travelling with a fixed zenith angle of  $\pm\theta_1$  (e.g.  $\theta_1 = 53^\circ$ ; Fu et al., 1997), and that the radiation is no longer entering the cloud from a single azimuth angle, but from

all azimuthal directions. As a result, the equivalent of (42) for the diffuse case is

$$f_{\text{diff}}^{ab} = L_{\text{diff}}^{ab} \tan(\theta_1)/c_a, \quad (46)$$

where  $L_{\text{diff}}^{ab}$  is the *effective length of cloud edge projected toward the diffuse radiation field*. We may use (40) but redefine  $\phi$  as the angle between the normal to the cloud edge and the direction of incidence of a particular ray of light. Since diffuse radiation by definition has a random azimuthal orientation,  $\phi$  will be uniformly distributed even if the cloud field has a preferred orientation with respect to some fixed coordinate system. This is mathematically equivalent to the case of direct radiation incident on a cloud edge with no preferred orientation described by (43), and so we have

$$L_{\text{diff}}^{ab} = L/(\pi A), \quad (47)$$

and in the case where the cloud edges are randomly oriented with respect to the sun we have  $L_{\text{diff}}^{ab} = L_{\text{dir}}^{ab}$ . In the case of linear contrails we had (45) for  $L_{\text{dir}}^{ab}$ , but to obtain the diffuse version we substitute  $L = 2X$  into (47) to get

$$L_{\text{diff}}^{ab} = \frac{2X}{\pi A} = \frac{c_b}{\pi W}. \quad (48)$$

The fact that the radiation has no preferred direction also means that the efficiency with which radiation travels from  $a$  to  $b$  is the same as from  $b$  to  $a$ , and so  $L_{\text{diff}}^{ba} = L_{\text{diff}}^{ab}$ .

## 5. Results

The effect of allowing lateral transport of radiation, which we refer to as the ‘‘3D effect’’, is now investigated. A simple radiation code has been created that calculates both direct and diffuse shortwave transfer based on the equations of section 3 and following the steps in Figure 3. It performs calculations using a single shortwave wavelength band with spectrally averaged optical properties and includes both 1D and 3D versions. In section 5a the behaviour of the new scheme is illustrated by computing the flux profiles resulting from each of the steps illustrated in Figure 3. Then in section 5b the 3D effect computed by the new scheme is compared to the results of full 3D radiation calculations reported in the literature. As will be shown, this is sufficient to demonstrate the potential of the technique, so we leave it to a future paper to apply this scheme in a full radiation code incorporating spectral bands.

### a. Profiles of flux through cloud layers

We begin by analysing the vertical distribution of shortwave radiative flux through a layer of cloud. A five-layer domain is used, with cloud partially filling the central three layers. The top and bottom layers of the domain are cloud-free and each has an optical depth of  $10^{-3}$ , an asymmetry factor of  $10^{-5}$  and single-scatter albedo of 0.99999. The physical depth of these cloud-free layers does not enter the calculation. Each of the

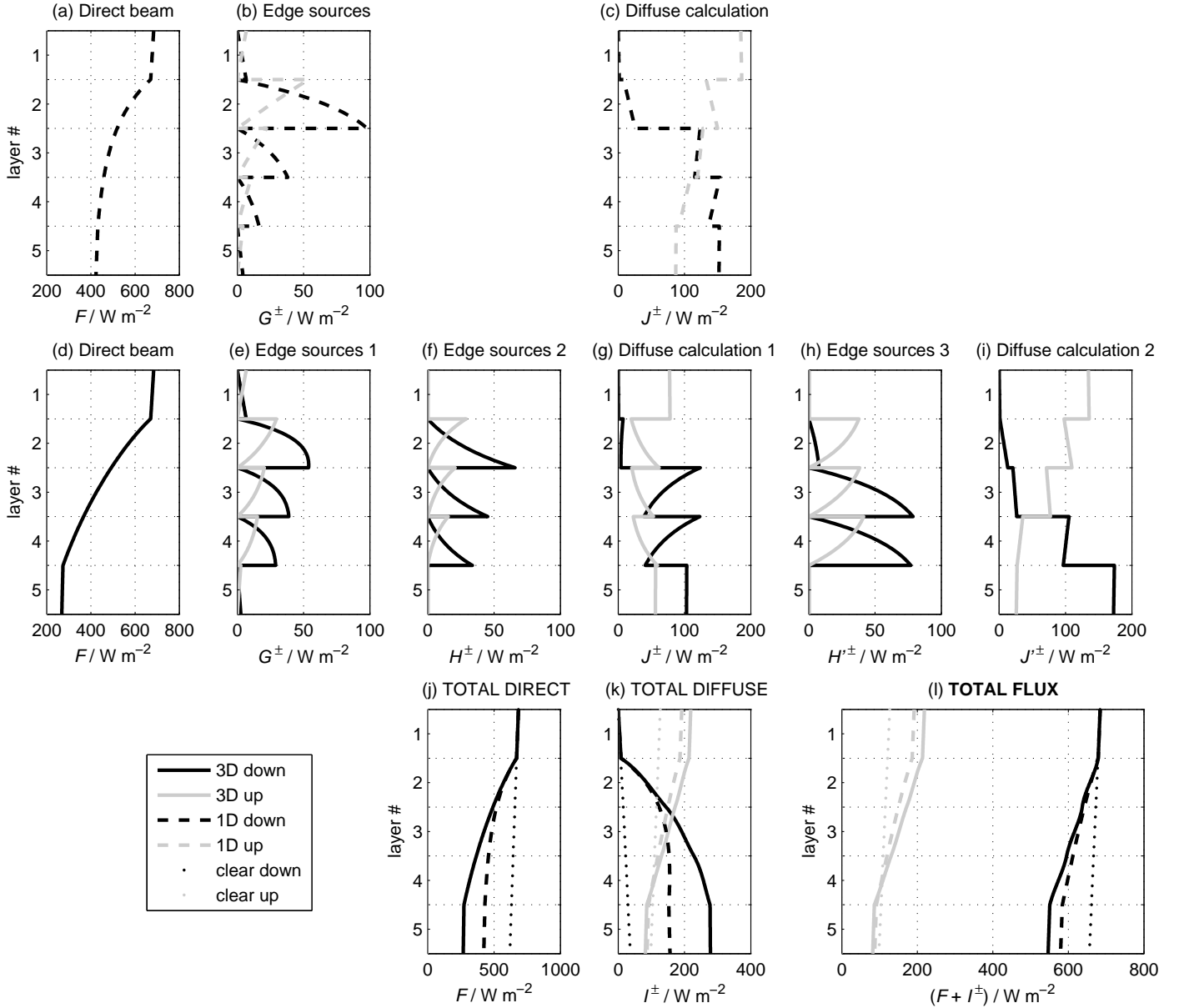


FIG. 7. Domain-mean (i.e. clear-sky plus cloudy) profiles of upward and downward direct and diffuse fluxes from each step of our simple radiation code. Panels (a) to (c) show the fluxes from each step of the 1D calculation (equivalent to most radiation schemes in current GCMs) corresponding to the steps laid out in panels (a) to (c) of Figure 3. Panels (d) to (i) show the same but for the 3D calculation, and corresponding to the same panels of Figure 3. The fluxes are for a five-layer model, with cloud situated in the central three layers (for the properties of the cloud, see the text). The panels in the bottom row show the total fluxes: panel (j) compares the 1D and 3D direct flux profiles from panels (a) and (d), while panel (k) compares the total diffuse flux profiles summed over all the diffuse steps. Panel (l) compares the sum of the direct and diffuse fluxes. Panels (j) to (l) also contain a profile of clear-sky flux for calculation of cloud radiative forcing.

three cloudy layers has a physical depth of  $\Delta z = 400$  m and a cloud fraction of  $c_b = 1/3$ . The clouds in each layer are maximally overlapped with an optical depth of 2, an asymmetry factor of 0.863, a single-scatter albedo of 0.999 and a vertical-to-horizontal aspect ratio  $r$  of one. Hence the total optical depth of the cloud in the domain is 6 and the aspect ratio of the whole cloud is three. Treating the clouds as cylindrical, this leads to effective cloud diameter of  $D_{\text{eff}} = \Delta z/r = 400$  m. Hence from (44), the effective length of cloud edge projected towards the direct and diffuse radiation per unit area is  $L_{\text{dir}}^{ab} = L_{\text{diff}}^{ab} = 0.00106 \text{ m}^{-1}$ . The surface albedo is 0.15, the total solar irradiance at the top of the atmosphere is assumed to be  $1,368 \text{ W m}^{-2}$  and in the calculations that follow we consider the case of a solar zenith angle of  $60^\circ$ .

For each layer, we extract the exponential coefficients describing the distribution of downward direct, downward diffuse and upward diffuse flux within that layer. These coefficients are extracted at each of the steps shown in Figure 3. This allows us not only to identify the 3D effect on the total fluxes, but also to partition the contributions to the total fluxes from each of the steps.

The resulting distribution of fluxes is shown in Figure 7. Panels (a) to (c) show the vertical profile of gridbox-averaged fluxes extracted from each step of the 1D calculation while panels (d) to (i) are for each step of the 3D calculation; thus the arrangement of these panels matches the steps shown schematically in Figure 3. The three panels in the bottom row show the effect on profiles of total direct (j), total diffuse (k) and overall total (l) fluxes when lateral transport is permitted. Within the cloudy layers, the flux profiles depicted are the sum of fluxes in the clear-sky and cloudy regions.

Panels (a) and (d) show the profile of direct flux through the domain, determined as a function of depth for each layer from (3) and (5) respectively. In an operational radiation scheme these fluxes would be evaluated only at layer boundaries, but here we have used these equations to show the vertical distribution of radiation within each layer. The effect of shortwave side illumination (discussed in section 2) to reduce the probability of direct sunlight from reaching the surface is immediately apparent from comparison of these two panels.

The fraction of the direct beam that is extinguished is scattered either into the upward or downward hemisphere (absorption is negligible, as we have set single-scatter albedo very close to one). We consider first the 1D calculation, in which the two-stream equations are analytically solved separately for each region (clear or cloudy) in each layer. In an operational radiation scheme, this step is purely to compute the exitant fluxes at the top and bottom of the layer due to scattering from the direct beam within the layer, which are used as “edge sources” in the following step. However, the implied vertical distribution of diffuse upwelling and downwelling flux can be calculated via (20) as a sum of four exponentials for each region of each layer; figure 7b depicts these profiles averaged over the clear and cloudy regions of each layer. As these profiles represent diffuse radia-

tion in each layer that originates only from scattering from the direct beam within that layer, the downward flux at layer top and upward flux at layer bottom must be zero, creating a discontinuous saw-tooth profile. A larger fraction of radiation scattered from the direct beam ends up in a downwelling beam simply because the positive asymmetry factor leads to a preference for forward scattering.

We next consider the 3D equivalent of this step, depicted in figure 7e. It can be seen that there is more diffuse radiation in layers 3 and 4, due to the direct beam able to enter the cloud in these layers through the cloud side, not just by passing through the cloud in layer 2 as in the 1D calculation. Another difference is that radiation is allowed to escape through cloud sides before reaching a layer boundary, achieved by using the modified version of  $\gamma_1$  defined in (19) in the 3D calculation.

The radiation that is lost by escape through cloud sides is then picked up and used as the source for a second diffuse calculation. Figure 7f shows the corresponding diffuse flux in each layer that has been transferred from an adjacent region. As for panel (e), this calculation is again performed separately within each region in each layer, giving it a similar saw-tooth shape. This part of the diffuse flux is also calculated using (20), but using source terms calculated from the flux profile in panel (e) via (28). To do this, the four exponentials used to describe the fluxes in each layer must be approximated to a single exponential using the method described in the appendix. This approximation changes the shape of the distribution in each layer from convex to concave, although it is found that this has a negligible effect on the final flux distribution.

These calculations of diffuse flux within a layer yield both downward and upward diffuse radiation emanating from the bottom and top of a layer, respectively, referred to in section 3b as the “edge sources”. The magnitude of these sources is equal to the size of the peaks in panel (b) for the 1D calculation, and the combined size of the peaks in panels (e) and (f) for the 3D calculation. These are then used as the edge sources for the calculation of the diffuse flux profile via (31) and (32) in section 3c. As before we consider first the 1D calculation, the results of which are shown in Figure 7c. The discontinuity of this profile is due to the fact that the edge sources in (31) and (32) act to inject energy from the previous step into the profile at the interfaces between layers. The shape of this profile has been reconstructed by first using the method of Shonk and Hogan (2008) to solve the linear system of equations while minimising the problem of anomalous horizontal radiation transport in the sub-cloud layer. This process yields the fluxes at the “downstream” side of each interface (i.e. just above the discontinuity in the upwelling profile and just below the discontinuity in the downwelling profile). Since we know that the size of the jump at each discontinuity is equal to the magnitude of the edge source, we can recover the fluxes at the “upstream” side, and then fit a two-exponential expression given by (20) to the interior of each layer (but with  $Z^\pm = 0$  since these represent interior sources). It may be a surprise that the part of a two-stream radiation scheme that involves

solving a linear system of equations is considering a discontinuous profile, but this is actually the assumption underlying all such schemes. Naturally, the full radiation profile is not discontinuous, and panel (k) of Figure 7 shows that when we sum the two contributions to the diffuse flux profile given in panels (b) and (c), we recover a continuous profile.

A similarly discontinuous profile to panel (c) is found in the 3D calculation depicted in panel (g). In the 3D case, this profile is computed accounting for lateral transport into the adjacent region by using modified  $R$  and  $T$  coefficients given by (29) and (30) using the effective  $\gamma_1$  defined in (19) to incorporate the extra loss of energy. This lost energy is injected into the adjacent region in the form of a source profile that is used in a further set of single-layer edge source calculations, which again produce a saw-tooth function for both upward and downward diffuse radiation as shown in panel (h). The resulting set of edge sources are then injected into a final multi-layer calculation, the results of which are shown in panel (i). Again, panels (h) and (i) are individually discontinuous, but when added together they provide a continuous function. Indeed, if we combine all contributions to the 3D diffuse flux profile from panels (e) to (i), the continuous result is depicted in panel (k).

The total downward direct fluxes for the 1D and 3D calculations are compared in panel (j), while the total upward and downward diffuse fluxes are compared in panel (k), the 1D diffuse flux being the sum of the fluxes in panels (b) and (c) and the 3D diffuse flux being the sum of the fluxes in panels (e) to (i). The corresponding total upwelling and downwelling fluxes (direct plus diffuse) are shown in panel (l), together with the clear-sky equivalent profiles.

We can identify both the effects of shortwave side illumination and shortwave side escape in these panels. The effect of shortwave side illumination is to cast larger shadows on the surface, hence allowing less direct radiation to reach the surface in the 3D case. In panel (j), the direct flux reaching the surface is reduced from  $422.8 \text{ W m}^{-2}$  to  $268.1 \text{ W m}^{-2}$ . Since the clear-sky direct flux is  $618.9 \text{ W m}^{-2}$ , the “3D effect” on the direct flux alone is to increase the CRF at the surface by 79%. Conversely, the effect of shortwave side escape is to increase the amount of both upward and downward diffuse radiation through the cloud layer, as scattered photons travel out of cloud sides. Net downward surface diffuse flux is increased from  $69.4 \text{ W m}^{-2}$  to  $196.3 \text{ W m}^{-2}$  in panel (k), which corresponds to a reduction in the CRF from diffuse flux alone of 97%, as the net downward clear-sky diffuse flux is  $-61.9 \text{ W m}^{-2}$ . At  $\theta_0 = 60^\circ$ , the shortwave side illumination has a larger impact, with a positive 3D effect on both surface and top-of-atmosphere cloud radiative forcing of 43% and 42% respectively.

#### b. Comparison with previous studies for varying solar zenith angle

Having shown that our simple radiation code can represent the effects of both shortwave side illumination and escape, we now perform simulations of the full radiative transfer calculations reported in the studies in Table 1. We use the same layer

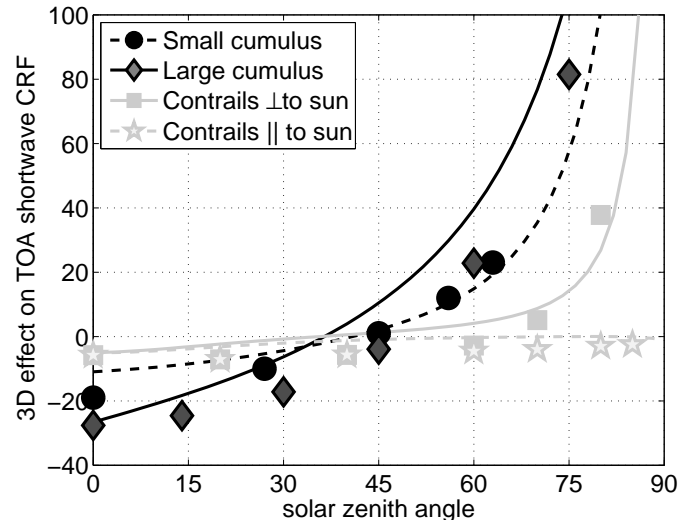


FIG. 8. The effect of 3D radiative transfer on shortwave top-of-atmosphere (TOA) cloud radiative forcing (CRF), versus solar zenith angle, for cumulus clouds and contrails, calculated using our modified two-stream scheme with a single layer of cloud having cloud fraction  $c_b$ , vertical-to-horizontal aspect ratio  $r$  and optical depth  $\delta$  shown in Table 1. Where reported, these values have been taken from the corresponding paper.

depth of 400 m, but reduce the domain to just three layers with the cloud represented in the middle layer. The cloud fractions and optical properties allotted to the cloudy region in the middle layer are taken from the values reported in the studies, again listed in Table 1. For each case, we perform three radiative transfer calculations: one using our new 3D method, one performing a traditional 1D two-stream calculation, and a clear-sky calculation to enable cloud radiative forcing (CRF) to be determined and hence the percentage shift to be found as in Figure 2.

The CRF for the 1D and 3D are compared with the reported values in Figure 8. The markers in this figure are exactly the same as in Figure 2, indicating the percentage effects on CRF of introducing 3D transport; the lines now show the CRF effects calculated using our code over all solar zenith angles. We see similarities between our calculated CRF shifts and those from the studies. In all cases, the compensating effects of shortwave side illumination and shortwave side escape can be clearly identified. For both types of cumulus cloud and the perpendicular contrails, at high solar zenith angles, inclusion of 3D effects reduces the CRF magnitude, which is consistent with the description of shortwave side escape in section 2. Conversely, for higher solar zenith angles, the shift is of opposite sign, with the inclusion of 3D effects increasing the magnitude of the CRF, agreeing with the sign of the change brought about by shortwave edge escape.

In comparison with the literature values on Figure 2, we see that, while agreement is not exact, the trends in 3D CRF shift

with solar zenith angle are the same. It is perhaps unrealistic to expect exact agreement between full 3D calculations and those made by our simple, one-band code. However, it is promising that the behaviour of the CRF shift with solar zenith angle is similar, with the switch of sign between high and low solar zenith angles. It should also be borne in mind that there is currently no representation of subgrid cloud inhomogeneity, as we have yet to incorporate Tripleclouds (Shonk and Hogan, 2008) in our two-stream scheme.

## 6. Summary and conclusions

In this paper we have described a novel method to account for the effects of 3D radiative transfer within a two-stream radiation code. First, extra terms are added to the equations describing the vertical distribution of direct radiation in each layer, to represent the lateral exchange of radiation between clear and cloudy regions. These are solved to obtain a modified version of Beer’s law. The effect of 3D transport on the diffuse radiation field is likewise tackled by introducing new terms into the two-stream equations, the solution of which requires several extra stages of computation as depicted graphically in Figure 3.

To test this idea, a simple single-band radiation scheme has been implemented that can model shortwave radiative transfer through a column of partially cloudy layers. The code has the ability to perform both traditional 1D calculations and full 3D calculations including lateral radiation transport using the method set out in this paper. The difference between the two enables the fractional change to the cloud radiative forcing (CRF) due to 3D effects to be quantified. This has been compared with the results of full 3D calculations reported in the literature for cumulus clouds and aircraft contrails. One study used the Monte Carlo method; the two others used the Spherical Harmonics Discrete Ordinate Method. Using the same cloud optical properties and cloud fraction as reported in these studies, we calculated the “3D effect” for a range of solar zenith angles. It was found that, while agreement between our results and their results was not exact, the dependence on solar zenith angle was similar. At low solar zenith angles, the effect of shortwave side escape was seen to dominate, leading to a negative effect on top-of-atmosphere CRF; at high solar zenith angles, the effect of shortwave side illumination was seen to dominate, leading to a positive effect on top-of-atmosphere CRF. For the cases we considered, the 3D effects varied from about  $-30\%$  up to over  $+100\%$ . These results confirm the importance of the first two mechanisms we identified in Figure 1. It should be noted that the only other fast method for 3D radiative transfer suitable for general circulation models (GCM), the Tilted Independent Column Approximation of Várnai and Davies (1999), cannot represent the second effect, shortwave side escape, and so would not be able to reproduce the negative 3D effect at low solar zenith angles.

Our scheme for incorporating 3D transport is around twice the computational expense of the equivalent 1D scheme. This is adequate for implementation in a GCM for research pur-

poses but, for operational weather forecasting or climate simulation, further work may be required to improve the efficiency. It should be pointed out that this is still orders of magnitude more efficient than the Monte Carlo method, which is the nearest alternative that could provide comparable or better accuracy.

A few further developments are required before the scheme would be ready for implementation in a GCM, or to be used off-line on reanalysis cloud fields to estimate the global impact of 3D radiative transfer:

- i. Our method needs to be implemented within a multi-band scheme for representing the spectral variation of gaseous absorption.
- ii. It would be ideal if the new 3D capability could be combined with a scheme for representing sub-grid cloud inhomogeneity. Since our method explicitly calculates the lateral flux between clear and cloudy regions, it would be most natural to apply it to the Tripleclouds method of Shonk and Hogan (2008) and to also compute the lateral flux between the optically thin and optically thick cloudy regions in each layer. Our 3D scheme is unfortunately incompatible with the Monte Carlo Independent Column Approximation of Pincus et al. (2003), since the independence of each column enables a different spectral band to be used in each column, making lateral transport between columns impossible.
- iii. The lateral radiation transfer needs to be extended to treat longwave radiation. This can be achieved simply by replacing the solar source term in (18) by the Planck function, which will allow the mechanism of longwave side exchange to be represented, depicted in the third panel of Figure 1.
- iv. Finally, section 4 showed how our method requires one number to specify the effective length of cloud edge within each gridbox,  $L_{diff}^{ab}$ , which for natural clouds can be assumed to be the same for direct and diffuse radiation. The challenge is then to estimate suitable values to use for this quantity within a GCM for particular cloud scenarios. As discussed in section 4, this information could be derived from observations (e.g. Jensen et al., 2008) or in some cases the model itself (e.g. Bechtold et al., 2001).

We would also be able to test whether the first two of these modifications lead to improved agreement between our method and the full 3D calculations in Figure 8.

### *Acknowledgments.*

We thank Robert Pincus for providing the necessary information to enable his paper to be included in Figures 2 and 8. This work was supported by NERC grant NE/G016038/1.

## APPENDIX

### Approximating the sum of exponentials by one exponential

In this appendix we show how a sum of  $n$  exponentials of the form

$$F(z) = \sum_{i=1}^n A_i \exp(a_i z) \quad (\text{A1})$$

may be approximated by a single exponential of the form

$$\hat{F}(z) = B \exp(bz), \quad (\text{A2})$$

in the range  $0 \leq z \leq z_1$ . This is necessary since (5) provides the vertical distribution of direct solar radiation as the sum of two exponentials, whereas in section 3b, it is required in the form of (17), i.e. (A2).

We specify that the single exponential should conserve both the zeroth and first moments of (A1), i.e. the total radiative energy  $E$  between  $z = 0$  and  $z = z_1$ , and the mean photon position  $\bar{z}$ . The total energy is given by

$$E = \int_0^{z_1} F(z) dz = \sum_{i=1}^n A_i (e^{a_i z_1} - 1) / a_i, \quad (\text{A3})$$

and

$$\bar{z} = \frac{1}{E} \int_0^{z_1} F(z) z dz = \frac{1}{E} \sum_{i=1}^n A_i [e^{a_i z_1} (a_i z_1 - 1) + 1] / a_i^2. \quad (\text{A4})$$

The energy may be conserved exactly and the mean position reproduced closely by (A2) if its coefficients are given by

$$b = \pi [\tan(\pi \hat{z}) - \pi (\hat{z}^3 - \hat{z}/4)]; \quad (\text{A5})$$

$$B = E b / (e^b - 1), \quad (\text{A6})$$

where  $\hat{z} = \bar{z} - 1/2$ .

## REFERENCES

- Barker, H. W., 1996: A parameterisation for computing grid-averaged solar fluxes for inhomogeneous marine boundary layer clouds. Part I: methodology and homogeneous biases. *Journal of the Atmospheric Sciences*, **53**, 2,289–2,303.
- Bechtold, P., E. Bazile, F. Guichard, P. Mascart, and E. Richard, 2001: A mass-flux convection scheme for regional and global models. *Quarterly Journal of the Royal Meteorological Society*, **127**, 869–886.
- Benner, T. C. and K. F. Evans, 2001: Three-dimensional solar radiative transfer in small tropical cumulus fields derived from high-resolution imagery. *Journal of Geophysical Research*, **106**, 14,975–14,984.
- Brooks, M. E., R. J. Hogan, and A. J. Illingworth, 2005: Parameterising the difference in cloud fraction defined by area and by volume as observed with radar and lidar. *Journal of the Atmospheric Sciences*, **62**, 2,248–2,260.
- Cahalan, R. F., W. Ridgway, W. J. Wiscombe, T. L. Bell, and J. B. Snyder, 1994: The albedo of fractal stratocumulus clouds. *Journal of the Atmospheric Sciences*, **51**, 2,434–2,455.
- DiGiuseppe, F. and A. M. Tompkins, 2003: Three-dimensional radiative transfer in tropical deep convective clouds. *Journal of Geophysical Research*, **108**, DOI: 10.1029/2003JD003392.
- Evans, K. F., 1998: The spherical harmonic discrete ordinate method for three-dimensional atmospheric radiative transfer. *Journal of the Atmospheric Sciences*, **55**, 429–446.
- Fu, Q., K. N. Liou, M. C. Cribb, T. P. Charlock, and A. Grossman, 1997: Multiple scattering parameterisation in thermal infra-red radiative transfer. *Journal of the Atmospheric Sciences*, **54**, 2,799–2,812.
- Gounou, A. and R. J. Hogan, 2007: A sensitivity study of the effect of horizontal photon transport on the radiative forcing of contrails. *Journal of the Atmospheric Sciences*, **64**, 1,706–1,716.
- Heidinger, A. K. and S. K. Cox, 1996: Finite-cloud effects in long-wave radiative transfer. *Journal of the Atmospheric Sciences*, **53**, 953–963.
- Jensen, M. P., A. M. Vogelmann, W. D. Collins, G. J. Zhang, and E. P. Luke, 2008: Investigation of regional and seasonal variations in marine boundary layer cloud properties from MODIS observations. *Journal of Climate*, **21**, 4,955–4,973.
- Joseph, J. H., W. J. Wiscombe, and J. A. Weinman, 1976: The delta-Eddington approximation for radiative flux transfer. *Journal of the Atmospheric Sciences*, **33**, 2,452–2,459.
- Killen, R. M. and R. G. Ellingson, 1994: The effect of shape and spatial distribution of cumulus clouds on longwave irradiance. *Journal of the Atmospheric Sciences*, **51**, 2,123–2,136.
- Liou, K. N., 1980: *An Introduction to Atmospheric Radiation*. Academic Press.
- Meador, W. E. and W. R. Weaver, 1980: Two-stream approximations to radiative transfer in planetary atmospheres: a unified description of existing methods and a new improvement. *Journal of the Atmospheric Sciences*, **37**, 630–643.
- Neggess, R. A., H. J. J. Jonker, and A. P. Siebesma, 2003: A multi-parcel model for shallow cumulus convection. *Journal of the Atmospheric Sciences*, **60**, 1,060–1,074.

- Pincus, R., H. W. Barker, and J. Morcrette, 2003: A fast, flexible, approximate technique for computing radiative transfer in inhomogeneous cloud fields. *Journal of Geophysical Research*, **108**, DOI: 10.1029/2002JD003322.
- Pincus, R., C. Hannay, and K. F. Evans, 2005: The accuracy of determining three-dimensional radiative transfer effects in cumulus clouds using ground-based profiling instruments. *Journal of the Atmospheric Sciences*, **62**, 2,284–2,293.
- Pomroy, H. R. and A. J. Illingworth, 2000: Ice cloud inhomogeneity: quantifying bias in emissivity from radar observations. *Geophysical Research Letters*, **27**, 2,101–2,104.
- Randall, D. A., et al., 2007: *Climate Change 2007: the Physical Science Basis. Contribution of Working Group I to the Fourth Assessment Report of the Intergovernmental Panel on Climate Change*, chap. 8: “Climate models and their evaluation”. Cambridge University Press.
- Shonk, J. K. P. and R. J. Hogan, 2008: Tripleclouds: an efficient method for representing cloud inhomogeneity in 1D radiation schemes by using three regions at each height. *Journal of Climate*, **21**, 2,352–2,370.
- Shonk, J. K. P. and R. J. Hogan, 2010: Effect of improving representation of horizontal and vertical cloud structure on the earth’s global radiation budget. Part II: the global effects. *Quarterly Journal of the Royal Meteorological Society*, **136**, 1,205–1,215.
- Shonk, J. K. P. and R. J. Hogan, 2011: Impact of improved representation of horizontal and vertical cloud structure in a climate model. *Climate Dynamics*, **in press**.
- Stuber, N., P. M. Forster, G. Rädcl, and K. P. Shine, 2006: The importance of the diurnal and annual cycle of air traffic for contrail radiative forcing. *Nature*, **441**, 864–867.
- Thomas, G. E. and K. Stamnes, 1999: *Radiative Transfer in the Atmosphere and Ocean*. Cambridge University Press.
- Tompkins, A. M. and F. DiGiuseppe, 2007: Generalising cloud overlap treatment to include solar zenith angle effects on cloud geometry. *Journal of the Atmospheric Sciences*, **64**, 2,116–2,125.
- Várnai, T. and R. Davies, 1999: Effects of cloud heterogeneities on short-wave radiation: comparison of cloud-top variability and internal heterogeneity. *Journal of the Atmospheric Sciences*, **56**, 4,206–4,224.
- Zhong, W., R. J. Hogan, and J. D. Haigh, 2008: Three-dimensional radiative transfer in mid-latitude cirrus clouds. *Quarterly Journal of the Royal Meteorological Society*, **134**, 199–215.
- Zuidema, P. and K. F. Evans, 1998: On the validity of the independent pixel approximation for boundary layer clouds observed during ASTEX. *Journal of Geophysical Research*, **103**, 6,059–6,074.